The crystal and defect structures of polar $KBiNb_2O_7$

ARTICLE

The crystal and defect structures of polar $KBiNb_2O_7$

Subhadip Mallick,[a] Weiguo Zhang,[b] Maria Batuk,[c] Alexandra S. Gibbs,[d] Joke Hadermann,[c] P. Shiv Halasyamani,[b] and Michael A. Hayward[a]*

$KBiNb_2O_7$ was prepared from $RbBiNb_2O_7$ by a sequence of cation exchange reactions which first convert $RbBiNb_2O_7$ to $LiBiNb_2O_7$, before $KBiNb_2O_7$ is formed by a further K-for-Li cation exchange. A combination of neutron, synchrotron X-ray and electron diffraction data reveal that $KBiNb_2O_7$ adopts a polar, layered, perovskite structure (space group *A*11*m*) in which the $BiNb_2O_7$ layers are stacked in a (0, ½, *z*) arrangement, with the K^+ cations located in half of the available 10-coordinate interlayer cation sites. The inversion symmetry of the phase is broken by a large displacement of the Bi^{3+} cations parallel to the *y*-axis. HAADF-STEM images reveal that $KBiNb_2O_7$ exhibits frequent stacking faults which convert the (0. ½, *z*) layer stacking to (½, 0, *z*) stacking and *vice versa*, essentially switching the *x*- and *y*-axes of the material. By fitting the complex diffraction peak shape of the SXRD data collected from $KBiNb_2O_7$ it is estimated that each layer has approximately an ~11% chance of being defective - a high level which is attributed to the lack of cooperative NbO_6 tilting in the material, which limits the lattice strain associated with each fault.

Introduction

Solid state compounds which exhibit non-centrosymmetric (NCS) crystal structures have been widely studied because they can exhibit physical properties such as ferroelectricity, piezoelectricity and second harmonic generation (SHG) which are forbidden by symmetry to centrosymmetric phases.[1, 2] However, the preparation of acentric solid phases is challenging, principally because NCS crystal structures tend to be thermodynamically unstable with respect to centric alternatives, as these latter high symmetry structures exhibit more efficient packing.

The conventional method used to stabilize acentric structures is to make use of an electronic instability of a chemical subunit to break the inversion symmetry of the underlying centrosymmetric framework of a material. For example, instabilities such as the second-order Jahn-Teller (SOJT) distortion of octahedrally coordinated d^0 transition metal cations (e.g. Ti^{4+} in $BaTiO_3$),[3-6] or the 'off-centring' distortions of ns^2 post-transition elements, often interpreted as stereoactive lone pairs (e.g. Bi^{3+} in $BiFeO_3$),[7-12] have been widely used to stabilize NCS crystal structures in complex oxide materials. However, the requirement to include these 'polar chemical species' limits the chemical constitution of NCS materials and makes it hard to include other properties such as magnetism in acentric phases.[13]

There has been much interest recently in a new class of acentric materials, the 'hybrid-improper' ferroelectrics, because their NCS crystal structures are not stabilized by specific polar chemical subunits. Instead the polar ground states of hybrid-improper ferroelectric phases are established by the presence of two non-polar structural distortion modes, which couple to, and stabilize a third polar distortion mode.[14, 15] This trilinear coupling of modes can stabilize polar NCS crystal structures without the assistance of local electronic instabilities, so offers the prospect of broadening the chemistry of NCS materials. It should be noted that the resulting polar materials are often referred to as 'hybrid-improper ferroelectric phases' because the ferroelectric polarisation which emerges at the paraelectric-to-ferroelectric phase transition of these materials need not be the primary order parameter of this phase transition.

The hybrid-improper mechanism has been observed to be responsible for the polar ground states of a number of $A_3B_2O_7$ n = 2 Ruddlesden-Popper oxide phases. In these systems two low-energy, cooperative tilting distortions of the BO_6 octahedra combine to stabilize a third polar distortion mode (usually a polar displacement of the *A*-cations) to yield polar and potentially ferroelectric phases. Thus, the polar ground state structures of $(Ca, Sr)_3Ti_2O_7$,[16] $(Ca, Sr)_3Sn_2O_7$ [17] $Sr_3Zr_2O_7$,[18] and $Ca_3Mn_2O_7$ [19] have been attributed to the hybrid-improper stabilization mechanism.

Layered perovskite oxides based on the $A'AB_2O_7$ n = 2 Dion-Jacobson framework have also been shown to exhibit polar structures stabilized by trilinear coupling.[20] For example, $CsNdM_2O_7$ and $RbNdM_2O_7$ (M = Nb, Ta) have been observed to adopt polar ground states, with ferroelectric switching reported for the two niobium phases.[21-23]

The extensive cation exchange chemistry exhibited by Dion-Jacobson phases allows a range of metastable layered perovskite phases to be prepared.[24] For example, the Rb^+

[a] Department of Chemistry, University of Oxford, Inorganic Chemistry Laboratory, South Parks Road, Oxford, OX1 3QR, UK.
[b] Department of Chemistry, University of Houston, 112 Fleming Building, Houston, Texas 77204-5003, USA.
[c] EMAT, University of Antwerp, Groenenborgerlaan 171, B-2020 Antwerp, Belgium.
[d] ISIS Facility, Rutherford Appleton Laboratory, Chilton, Oxon OX11 0QX, UK.
Electronic Supplementary Information (ESI) available: [details of any supplementary information available should be included here]. See DOI: 10.1039/x0xx00000x

cations in $RbNdM_2O_7$ (M = Nb, Ta) can be exchanged for K^+, Na^+ or Li^+, allowing the whole range of $A'NdNb_2O_7$ (A' = Cs, Rb, K, Na, Li) materials to be investigated.[25, 26] This reveals that $LiNdM_2O_7$ and $NaNdM_2O_7$ adopt pseudo Ruddlesden-Popper structures with the lithium materials exhibiting polar ground states stabilized by trilinear coupling, in contrast to the centrosymmetric structures of the sodium phases – a difference which can be attributed to the differing cation ordering patterns present in the contrasting materials.[25] $KNdNb_2O_7$ and $KNdTa_2O_7$ adopt layered perovskite structures with an unusual (0, ½, z) stacking of the perovskite sheets which are separated by 6-coordinate prismatic K^+ cations.[26] Structural analysis reveals these $KNdM_2O_7$ materials are polar, but in this instance the acentric ground state is stabilized by a 'conventional' SOJT distortion of the MO_6 units.

The conventional polar distortions of the $KNdM_2O_7$ phases highlight the fact that many of the complex oxides which exhibit hybrid-improper polar ground states also contain 'polar chemical species', such as octahedrally coordinated d^0 transition-metal cations. Thus, in principle, these compounds could adopt polar structures stabilized by the SOJT distortions of these polar chemical groups, which are in competition with the observed polar structures stabilized by trilinear coupling. This competition can be seen clearly in the two pseudo Ruddlesden-Popper phases $Li_2La(TaTi)O_7$ and $Na_2La(TiTa)O_7$ in which the polar distortion of the lithium phase is stabilized by trilinear coupling, in contrast to that of the sodium phase which is consistent with a SOJT stabilization mechanism.[27]

Recently, to investigate the effect of including ns^2 post-transition metal cations in hybrid-improper polar phases, we reported the structures of $NaBiNb_2O_7$ and $LiBiNb_2O_7$ which were prepared by cation exchange from the Dion-Jacobson phase $RbBiNb_2O_7$.[28] Here we complete the $A'BiNb_2O_7$ series with an investigation of $KBiNb_2O_7$.

Experimental

Synthesis

Samples of $KBiNb_2O_7$ were prepared by first synthesising $RbBiNb_2O_7$, converting this material to $LiBiNb_2O_7$ via Li-for-Rb cation exchange,[28] and finally forming $KBiNb_2O_7$ via a K-for-Li cation exchange reaction. Specifically, polycrystalline samples of $RbBiNb_2O_7$ were prepared by a solid-state ceramic synthesis method from suitable stoichiometric ratios of Bi_2O_3 (99,995%) and Nb_2O_5 (99.9985%, dried at 900 °C), which were ground together in an agate pestle and mortar and combined with 50 % excess (to compensate for the loss due to volatilization at high temperature) of Rb_2CO_3 (99.8%). These mixtures were then placed in open-ended silica tubes and heated at 600 °C in air for 12 h. The samples were then reground and heated at 1000 °C for 6 h then 12 h and 2 further periods of 4 h with regrinding between heating cycles. Finally, the powder samples were washed with distilled water to remove any excess rubidium oxide and then dried in air at 120 °C for 12 h. This heating regime was required to avoid the formation of $BiNbO_4$.

$LiBiNb_2O_7$ was synthesized as described previously [28] by reacting $RbBiNb_2O_7$ with 10 mole-equivalents of $LiNO_3$ (99.98 %) in open ended silica tubes at 360 °C in air, for two periods of 48 h. Between heating cycles, samples were washed with distilled water, dried for 12 h at 120 °C in air and then mixed with a further 10 mole-equivalents of $LiNO_3$. After the final heating step, all samples were washed with distilled water to remove the $LiNO_3$ and then dried for 12 h at 120 °C in air.

$KBiNb_2O_7$ was synthesized by reacting $LiBiNb_2O_7$ with 10 mole-equivalents of KNO_3 (99.995%) in open ended silica tubes at 400 °C in air, for two periods of 48 h. Between heating cycles, samples were washed with distilled water, dried for 12 h at 120 °C in air and then mixed with a further 10 mole-equivalents of KNO_3. After the final heating step, all samples were washed with distilled water to remove the excess KNO_3 and then dried for 12 h at 120 °C in air.

Characterisation

X-ray powder diffraction data were collected using a PANalytical X'pert diffractometer incorporating an X'celerator position-sensitive detector (monochromatic Cu $K\alpha_1$ radiation). High-resolution synchrotron X-ray powder diffraction (SXRD) data were collected using the I11 instrument at the Diamond Light Source Ltd. Diffraction patterns were collected using Si-calibrated X-rays with an approximate wavelength of 0.825 Å from samples, sealed in 0.3 mm diameter borosilicate glass capillaries. Time-of-flight neutron powder diffraction (NPD) data were collected using the HRPD diffractometer at the ISIS neutron source from the samples loaded in 8 mm vanadium cans. Rietveld refinements were performed using the TOPAS Academic (V6).[29] The particle-size dependent second harmonic generation (SHG) response of samples was measured by grinding sintered pellets of material and then sieving the resulting powders into distinct particle size ranges (<20, 20-45, 45-63, 63-75, 75-90, 90-125 μm). SHG intensity was then recorded from each particle size range and compared to a standard sample of KH_2PO_4 (KDP) in the same particle size ranges. No index matching fluid was used in any of the experiments. A detailed description of the experimental setup and process has been reported previously.[30]

Electron diffraction (ED) patterns were acquired on a FEI Tecnai transmission electron microscope (TEM) operated at 200 kV.

High angle annular dark field (HAADF) scanning transmission electron microscopy (STEM) images were acquired using a probe aberration corrected FEI Titan 80-300 "cubed" microscope operated at 300 kV. Samples for TEM analysis were prepared in an argon-filled glove box by dipping a copper TEM grid into the ground dry powder. The grids were then transferred into the microscope using a vacuum transfer holder. Simulated HAADF-STEM images were calculated using the QSTEM software.["Determination of core structure periodicity and point defect density along dislocations": C. Koch, Ph.D. Thesis, Arizona State University, 2002.]

Results

Synthesis of $KBiNb_2O_7$

$KBiNb_2O_7$ could not be prepared by direct high-temperature synthesis. Reaction of K_2CO_3, Bi_2O_3 and Nb_2O_5 at 1100 °C primarily yielded the tetragonal tungsten bronze phase $K_2BiNb_5O_{15}$,[31] indicating that the desired layered perovskite phase is metastable with respect to a mixture of the tetragonal tungsten bronze phase and Bi_2O_3. $KBiNb_2O_7$ could be prepared

via K-for-Li cation exchange of $LiBiNb_2O_7$, as described above. It should be noted that unlike $KNdNb_2O_7$,[26] $KBiNb_2O_7$ could not be prepared via direct K-for-Rb cation exchange of the corresponding $RbANb_2O_7$ phase, with the synthesis of $KBiNb_2O_7$ only achieved via the reaction sequence $RbBiNb_2O_7$ to $LiBiNb_2O_7$ to $KBiNb_2O_7$.

Structural characterisation of $KBiNb_2O_7$

High resolution SXRD and NPD data collected from $KBiNb_2O_7$ was initially indexed using a monoclinic unit cell (a = 3.847 Å, b = 3.840 Å, c = 22.193 Å, γ = 90.80°). This unit cell is consistent with the aristotype unit cell of a (0, ½, z) stacked n = 2 layered perovskite.[32-34] However, on close inspection a series of small diffraction peaks were observed (Figure S1, Supporting Information) which could only be indexed using an expanded unit cell (a = 7.694 Å, b = 3.840 Å, c = 22.193 Å, γ = 90.80°) which is an $a' \approx 2a$, $b' \approx b$, $c' \approx c$ geometric expansion of the aristotype unit cell, with extinction conditions consistent with an A-centred unit cell.

Electron diffraction (ED) patterns collected from $KBiNb_2O_7$ (Figure 1) show streaking along c*, indicative of stacking faults in the material (*vide infra*). Analysis of these patterns confirms the $a' \approx 2a$, $b' \approx b$, $c' \approx c$ unit cell obtained from the SXRD and NPD data, with extinction conditions consistent with A-centring.

Particle-size dependent SHG data (Figure 2) reveals $KBiNb_2O_7$ has an SHG activity which is approximately 1.5 times that of KDP, and thus has a non-centrosymmetric crystal structure.

Combining the information above, we can deduce that $KBiNb_2O_7$ adopts a crystal structure described in an A-centred, non-centrosymmetric monoclinic space group. This gives 3 candidates: $A11a$ (#9), $A11m$ (#8) and $A112$ (#5) with unit cell settings chosen to preserve the z-axis as the stacking direction. Structural models were constructed in these three space groups and refined against the NPD data collected at room temperature. The diffraction data show strongly *hkl*-dependent peak shape as shown in Figure S2 in the Supporting Information, which arises from stacking faults in the material as discussed later. At this stage of the structural refinement no attempt was made to include stacking faults in the structural model, with the *hkl*-dependent peak width modelled by a 6th order spherical harmonic,[35] which led to a significant improvement in the fit to the data.

A comparison of fitting statistics reveals that the $A112$ model fits the data poorly (wR_p = 10.2) and yields a chemically implausible structure for $KBiNb_2O_7$, so this model was rejected. The fitting parameters from the refinement of $A11m$ (wR_p = 8.43) and $A11a$ (wR_p = 8.50) symmetry models are comparable.

A close inspection of the refined $A11a$ model reveals many atoms located on general symmetry positions refine to locations for which the z-parameter is zero, within error, consistent with the presence of a mirror plane perpendicular to the z-axis at this position, suggesting the $A11m$ space group is a better symmetry description of $KBiNb_2O_7$. In addition, an analysis of the bond valence sums (BVS) [36, 37] revealed the $A11m$ model yielded more chemically realistic values for the K^+, Nb^{5+} and Bi^{3+} cations than the $A11a$ model. These observations

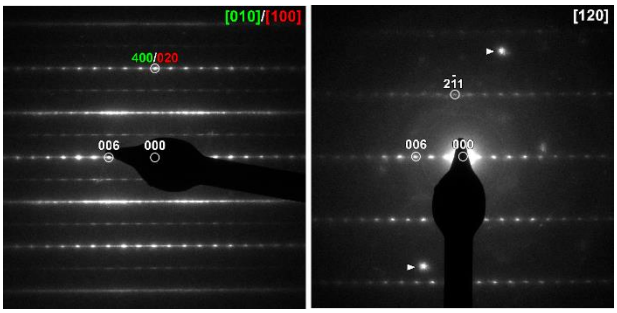

Figure 1. Electron diffraction patterns collected from $KBiNb_2O_7$. The presence of 'axis-switch' stacking faults means the [010] and [100] zone axes are superimposed. The marked spots in [120] are due to an overlap with another crystal.

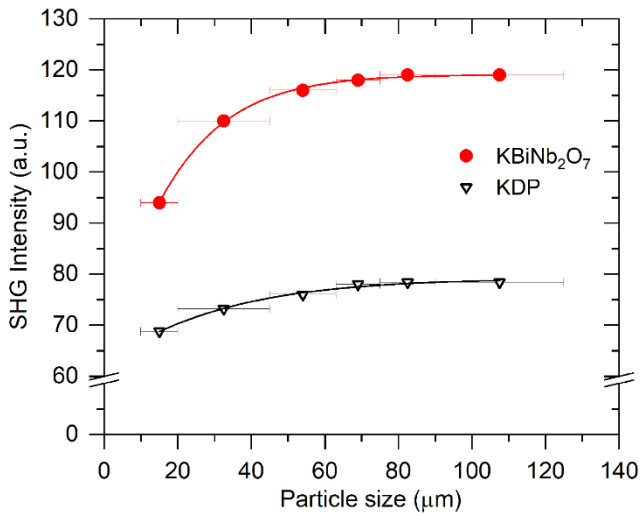

Figure 2. SHG activity as a function of particle size for $KBiNb_2O_7$ compared to a KDP standard.

indicate that the $A11m$ model is a better choice for the room temperature structure of $KBiNb_2O_7$ than the $A11a$ symmetry model. Full details of the refined $A11m$ model of $KBiNb_2O_7$ are given in Table 1, with selected bond lengths in Table S2 and a plot of the observed and calculated data shown in Figure 3. It should be noted that the rather large thermal displacement parameters detailed in Table 1 are attributed to the stacking disorder exhibited by the phase, as described below.

Microstructural characterisation of $KBiNb_2O_7$

The SXRD and NPD data collected from $KBiNb_2O_7$ exhibit very strong *hkl*-dependent broadening, which can be seen clearly in Figure 3 and accounts for the relatively poor fit to the data. In addition, ED patterns show extensive streaking parallel to the c* direction (Figure 1). Together these observations suggest $KBiNb_2O_7$ exhibits some variety of stacking fault disorder. To investigate the nature of the stacking faults a series of HAADF-STEM images were collected.

As noted above, the aristotype n = 2, (0, ½, z) layered perovskite structure adopted by KAB_2O_7 phases can be considered as a hybrid of the (0,0, z) stacked Dion-Jacobson framework and the (½, ½, z) stacked Ruddlesden-Popper framework. HAADF-STEM images collected from $KBiNb_2O_7$ show that the $BiNb_2O_7$ perovskite sheets in $KBiNb_2O_7$ adopt an evenly spaced stacking

Table 1. Parameters from the structural refinement of $KBiNb_2O_7$ against NPD data collected at room temperature.

Atom	Site	*x*	*y*	*z*	Occ.	B_{iso} (Å^2)
K1	4*b*	0.003(3)	0.967(6)	0.1963(6)	½	3.2(1)
K2	4*b*	0.501(3)	0.966(5)	0.1965(5)	½	3.2(1)
Bi1	2*a*	0.0204(1)	0.066(4)	0	1	6.3(4)
Bi2	2*a*	0.5205(1)	0.932(4)	0	1	6.3(4)
Nb1	4*b*	0.251(1)	0.001(1)	0.3958(1)	1	4.2(1)
Nb2	4*b*	0.750(1)	0.999(1)	0.3957(1)	1	4.2(1)
O1	2*a*	0.214(1)	0.524(4)	0	1	5.3(2)
O2	2*a*	0.713(1)	0.475(4)	0	1	5.3(2)
O3	4*b*	0.001(1)	0.962(5)	0.4130(6)	1	6.8(3)
O4	4*b*	0.499(1)	0.038(5)	0.4132(5)	1	6.8(3)
O5	4*b*	0.275(1)	0.009(4)	0.3160(3)	1	5.9(2)
O6	4*b*	0.774(1)	0.008(4)	0.3159(3)	1	5.9(2)
O7	4*b*	0.2907(9)	0.993(1)	0.0889(2)	1	4.3(2)
O8	4*b*	0.7905(9)	0.994(1)	0.0888(2)	1	4.3(2)

$KBiNb_2O_7$ – space group *A*11*m* (#8)
a = 7.6735(3) Å, *b* = 3.8437(2) Å, *c* = 22.1699(9)Å, γ = 90.806(1),
V = 653.83(5)Å^3, Formula weight = 545.89 g mol^{-1}, Temperature: 298 K
R_p = 7.54 %, $_wR_p$ = 8.43 %

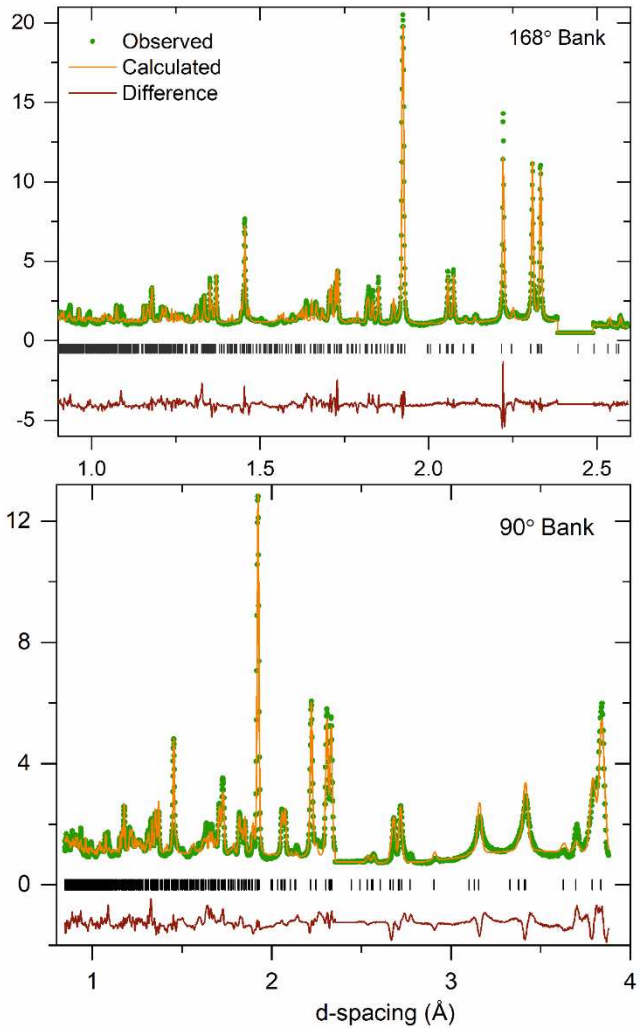

Figure 3. Observed, calculated and difference plots from the structural refinement of $KBiNb_2O_7$ against NPD data collected at room temperature. Excluded regions remove contributions from an unidentified impurity phase.

sequence. However, close inspection shows that the stacking exhibits frequent 'faults' in which the (0, ½, *z*) stacking changes to a (½, 0, *z*) and *vice versa*, as shown in Figure 4. This type of stacking fault corresponds to a switching of the *x*- and *y*-axes in the aristotype structure, and from the HAADF-STEM images these faults appear to be prevalent throughout the $KBiNb_2O_7$ sample measured.

In an attempt to quantify the frequency of this stacking fault, the structural model obtained from the NPD data was modified to introduce this 'axis-switch' stacking fault with a frequency defined by a variable, *FF* (Fault Frequency), which describes the probability that at any potassium layer there will be a change from (0, ½, *z*) stacking to (½, 0, *z*) stacking or *vice versa*, as described in detail in the Supporting Information. A series of models with different values of *FF* were refined against the SXRD data, whilst keeping the atomic coordinates of the model static, to find the value of *FF* which best fitted the data. The introduction of this fault description led to a great improvement in the fit to the data as shown in Figure 5. As shown in Figure 6, the best fit to the SXRD data was obtained with a value of *FF* = 0.09, which corresponds to a 9% chance of a stacking fault occurring between any particular pair of perovskite double sheets. This faulting probability appears to be in line with the number of faults observed in the HAADF-STEM images. Attempts to perform an analogous analysis using the NPD data were hampered by the complex double-exponential peak shape of the time-of-flight instrument.

Discussion

$KBiNb_2O_7$ adopts a layered structure in which the $BiNb_2O_7$ perovskite double sheets are stacked in a (0, ½, *z*) manner, with the K^+ cations adopting a disordered arrangement within half of the 10-coordinate sites in the interlayer region. The $BiNb_2O_7$ sheets do not adopt a cooperative tilting distortion of the NbO_6 units, but are distorted by a large alternating displacement of the Bi^{3+} cations along the *y*-axis, as shown in Figure 7. This low-symmetry, polar crystal structure differs markedly from other members of the *A*'$BiNb_2O_7$ (*A*' = Cs, Rb, Na, Li) series. We can gain some insight into the interactions which lead to this low symmetry structure by examining how the structures of other phases in the *A*'$BiNb_2O_7$ series, and related A'$NdNb_2O_7$ series, evolve on changing the *A*'-cation.

As described previously,[21, 25, 26] the stacking of the $NdNb_2O_7$ perovskite sheets and the cooperative tilting of the NbO_6 units in the *A*'$NdNb_2O_7$ series of layered perovskite phases, can be rationalised on the basis of simultaneously satisfying the bonding requirements of both the *A*' and Nd^{3+} cations.

It can be observed that as the size of the *A*'-cations declines across the *A*'$NdNb_2O_7$ series, so does the A' coordination number in the resulting framework, from 8-fold (*A*' = Cs, Rb) to 6-fold (*A*' = K) to 4-fold (*A*' = Na, Li). This change is facilitated by a change in the layer stacking type, from (0, 0, *z*) Dion-Jacobson stacking (*A*' = Cs, Rb) to (0, ½, *z*) stacking (*A*' = K) to (½, ½, *z*) Ruddlesden-Popper stacking (*A*' = Na, Li). Thus, the structural evolution of the *A*'$NdNb_2O_7$ series can be simply rationalized on the basis of the *A*'-cation size.

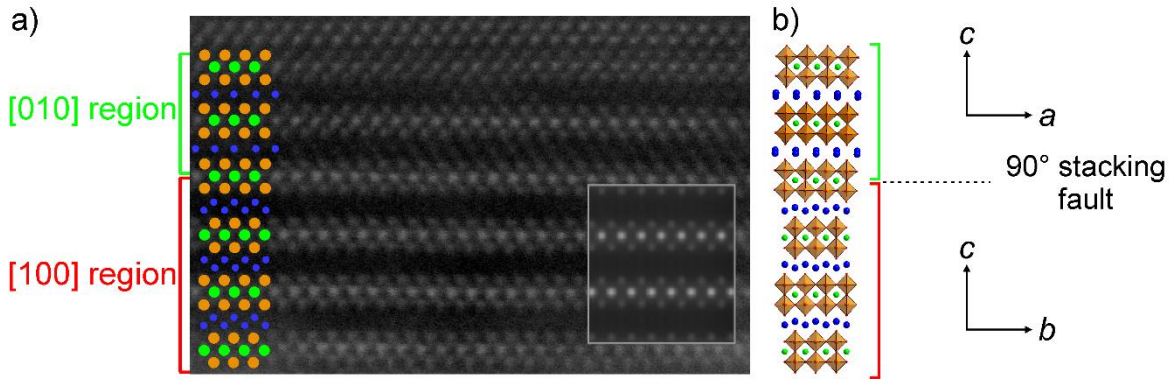

Figure 4. a) HAADF-STEM image collected from $KBiNb_2O_7$. Green bracket shows stacking of $BiNb_2O_7$ sheets corresponding to [010] zone. Red bracket shows stacking corresponding to [100] zone. Superimposed spheres correspond to Bi (green), Nb (orange) and K (blue) atoms. Inset shows simulated [100] image of $KBiNb_2O_7$. b) Representation of the 90° stacking fault in $KBiNb_2O_7$.

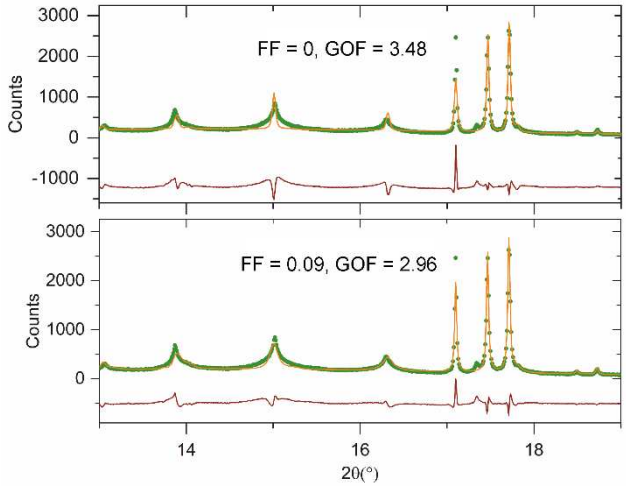

Figure 5. Observed calculated a difference plots from the structural refinement of $KBiNb_2O_7$ (bottom) with and (top) without 90° stacking fault description.

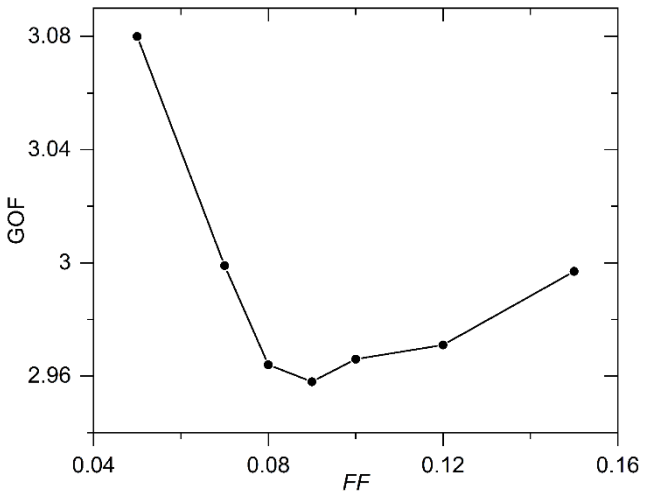

Figure 6. Plot of Goodness of fit (GOF) parameter against Fault Frequency (FF) determined by fitting to SXRD data.

A similar sequence of structures is adopted by some members of the *A*'$BiNb_2O_7$ series, with the *A*' = Cs, Rb, Li phases being

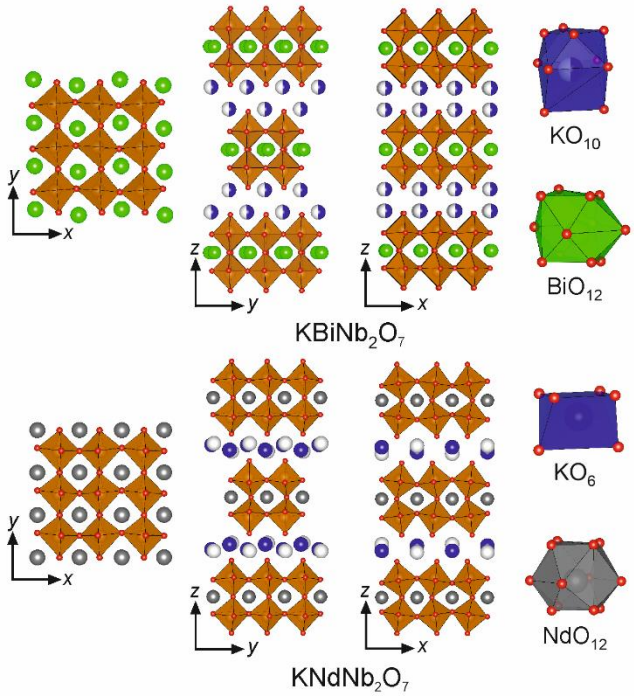

Figure 7. The crystal structures of $KBiNb_2O_7$ and $KNdNb_2O_7$. Purple, green, orange, grey and red spheres represent K, Bi, Nb, Nd and O respectively.

isostructural to their *A*'$NdNb_2O_7$ analogues. These isostructural relationships are perhaps a little unexpected given the preference for $6s^2$ Bi^{3+} cations to adopt asymmetric coordinations in contrast to the more symmetric environments favored by Nd^{3+}. However, in the case of the Cs, Rb and Li phases, the large magnitude tilting distortions exhibited by the ANb_2O_7 sheets, which are required to simultaneously satisfy the coordination requirements of the *A*' and Nd^{3+} cations, lower the symmetry of the *A*-cation sites (by way of the trilinear coupled hybrid improper mechanism)[14, 20] to the ..*m* point symmetry favored by Bi^{3+}.[28] Thus, perhaps coincidentally, Nd^{3+} and Bi^{3+} can be accommodated in the same structural frameworks, despite

the contrasting features (Nd^{3+} small size; Bi^{3+} non-spherical geometry) of the two ions.

However, the differing coordination preferences of Nd^{3+} and Bi^{3+} do lead to a small difference in the structures of $NaNdNb_2O_7$ and $NaBiNb_2O_7$.[25, 28] Both $NaANb_2O_7$ phases adopt a (½, ½, *z*) stacking of the ANb_2O_7 layers, with Na^+ cations ordered in 4-coordinate sites in the interlayer region. However, the relatively large size of Na^+ means that $NaNdNb_2O_7$ adopts a small magnitude $a^-b^0c^0$/ $b^0a^-c^0$ tilting distortion (space group $P4_2/mnm$) with the Nd^{3+} cation accommodated on a site of *m*.2*m* point symmetry. This site symmetry appears to be incompatible with the coordination requirements of Bi^{3+} as $NaBiNb_2O_7$ adopts a much larger magnitude $a^-a^-c^+$/ a^-a^--c^+ tilting distortion (space group $P2_12_12_1$), despite Bi^{3+} being larger than Nd^{3+}, which lowers the point symmetry of the Bi^{3+} cations to that of a general position, yielding an asymmetric bismuth coordination environment, suggesting that the change in structure occurs in response to an off-centring distortion of the Bi^{3+} cations.

In light of the analysis above, we can rationalise the much more significant structural differences between $KNdNb_2O_7$ and $KBiNb_2O_7$. $KNdNb_2O_7$ adopts a (0, ½, *z*) stacking pattern of the $NdNb_2O_7$ sheets, which themselves exhibit a cooperative $a^0b^+c^0$/a^0-b^+c^0 tilting scheme to best accommodate the K^+ cations, which are ordered within half of the available 6-coordinate trigonal prismatic sites in the interlayer region of the structure as shown in Figure 7. As noted above, $KBiNb_2O_7$ also exhibits a (0, ½, *z*) stacking pattern of the ANb_2O_7 perovskite sheets, however the remaining structural details are strongly contrasting: the K^+ cations in $KBiNb_2O_7$ adopt a disordered arrangement within half of the 10-coordinate sites in the interlayer region and no cooperative tilting distortion is observed in the $BiNb_2O_7$ layers, which are instead distorted by a large alternating displacement of the Bi^{3+} cations, shown in Figure 7.

Again the structural differences between the neodymium and bismuth phases can be attributed to the coordination preferences of the Nd^{3+} and Bi^{3+} cations. The $a^0b^+c^0$/a^0-b^+c^0 tilting distortion exhibited by the $NdNb_2O_7$ sheets in $KNdNb_2O_7$ results in a 222 point symmetry site for the Nd^{3+} cations. As noted above, such a high symmetry site appears to be incompatible with the asymmetric coordination environments adopted by Bi^{3+} - a statement supported by the observation that the Bi^{3+} sites in $KBiNb_2O_7$ have ..*m* point symmetry. Thus, we can attribute the change in structure on replacing Nd^{3+} with Bi^{3+} within the $KANb_2O_7$ framework to the preference for asymmetric environments exhibited by $6s^2$ Bi^{3+} cations. It is worth noting however, that in contrast to the simple change in tilting pattern on Bi^{3+}-for-Nd^{3+} substitution exhibited by the $NaANb_2O_7$ framework, the potassium system undergoes a much more dramatic change in structure on the introduction of bismuth, with the K^+ coordination site and the ANb_2O_7 layer distortion changing. The resulting structure of $KBiNb_2O_7$ has a highly distorted $BiNb_2O_7$ layer in which the NbO_6 units are deformed from their expected octahedral geometry. This low symmetry arrangement suggests that it is difficult to simultaneously satisfy the coordination preference of K^+ and Bi^{3+} simultaneously in this (0, ½, *z*) framework, with the observed structure being the best compromise. As a consequence the inversion symmetry breaking in the non-centrosymmetric structure of $KBiNb_2O_7$ can be attributed to an SOJT-like distortion driven by the $6s^2$ electronic configuration of Bi^{3+}, in contrast to $KNdNb_2O_7$ where the inversion symmetry breaking is attributed to an SOJT-like distortion driven by the Nb^{5+} cations.[26]

A further striking feature exhibited by $KBiNb_2O_7$ is the axis-switch stacking fault in which the (0, ½, *z*) stacking changes to (½, 0, *z*) stacking and vice versa. In principle, such a stacking fault should apply significant lattice strain to the materials. However, due to the lack of a cooperative NbO_6 tilting distortion, the lattice parameters of $KBiNb_2O_7$ are close to being metrically tetragonal (if the *x*-axis doubling due to the alternating Bi displacement is ignored) so the strain associated with the faulting should be minimal. Thus we can see that the prevalent axis-switch faults can be attributed to features of the crystal structure of the material.

Conclusions

The facile cation-exchange reactions exhibited by Dion-Jacobson phases allow a wide range of metastable, layered perovskite oxide phases to be prepared. In the case of the *A*'$BiNb_2O_7$ series this allows the competition between alternative polar grounds states stabilized by either trilinear coupling, the SOJT distortions of $Nb^{5+}O_6$ units, or the off-centring distortions of $6s^2$ Bi^{3+}, to be studied.

In the case of $KBiNb_2O_7$, we observe this phase is highly metastable, and can only be prepared through a 3-step reaction sequence. The phase produced differs significantly from the analogous Nd^{3+} phase, $KNdNb_2O_7$, both in the local coordination of the K^+ cations and the deformation of the ANb_2O_7 perovskite double sheets. In addition $KBiNb_2O_7$ exhibits extensive 'axis-switch' stacking faults. These features combine to highlight the dominant influence of the off-centring distortions of the Bi^{3+} cations in this phase.

Author Contributions

SM prepared the samples and performed the structural analysis, WZ and PSH collected the SHG data, MB and JH collected the microscopy data, ASG assisted with the collection of the NPD data, MAH conceived the study, wrote the manuscript and supervised the study.

Conflicts of interest

There are no conflicts to declare.

Acknowledgements

Experiments at the Diamond Light Source were performed as part of the Block Allocation Group award "Oxford/Warwick Solid State Chemistry BAG to probe composition-structure-property relationships in solids" (EE18786). Experiments at the

ISIS pulsed neutron facility were supported by a beam time allocation from the STFC (RB 2000148). SM thanks Somerville College for an Oxford Ryniker Lloyd scholarship. PSH and WZ thank the National Science Foundation (DMR-2002319) for support.

Notes and references

1. M. E. Lines and A. M. Glass, *Principles and Applications of Ferroelectrics and Related Materials*, Oxford University Press, Oxford, 1991.
2. F. J. Nye, *Physical Properties of Crystals*, Oxford University Press, Oxford, UK, 1957.
3. R. E. Cohen, *Nature*, 1992, **358**, 136-138.
4. M. Kunz and I. D. Brown, *J. Solid State Chem.*, 1995, **115**, 395-406.
5. S. K. Kang, H. Tang and T. A. Albright, *J. Am. Chem. Soc.*, 1993, **115**, 1971-1981.
6. R. G. Pearson, *Theochem-Journal of Molecular Structure*, 1983, **12**, 25-34.
7. I. Lefebvre, M. Lannoo, G. Allan, A. Ibanez, J. Fourcade, J. C. Jumas and E. Beaurepaire, *Phys. Rev. Lett.*, 1987, **59**, 2471-2474.
8. I. Lefebvre, M. A. Szymanski, J. Olivier-Fourcade and J. C. Jumas, *Phys. Rev. B*, 1998, **58**, 1896-1906.
9. R. Seshadri and N. A. Hill, *Chem. Mater.*, 2001, **13**, 2892-2899.
10. M. W. Stoltzfus, P. M. Woodward, R. Seshadri, J. H. Klepeis and B. Bursten, *Inorg. Chem.*, 2007, **46**, 3839-3850.
11. G. W. Watson and S. C. Parker, *J. Phys. Chem. B*, 1999, **103**, 1258-1262.
12. G. W. Watson, S. C. Parker and G. Kresse, *Phys. Rev. B*, 1999, **59**, 8481-8486.
13. N. A. Hill, *J. Phys. Chem. B*, 2000, **104**, 6694-6709.
14. N. A. Benedek and C. J. Fennie, *Phys. Rev. Lett.*, 2011, **106**, 107204.
15. N. A. Benedek, J. M. Rondinelli, H. Djani, P. Ghosez and P. Lightfoot, *Dalton Trans.*, 2015, **44**, 10543-10558.
16. Y. S. Oh, X. Luo, F. T. Huang, Y. Z. Wang and S. W. Cheong, *Nat. Mater.*, 2015, **14**, 407-413.
17. S. Yoshida, H. Akamatsu, R. Tsuji, O. Hernandez, H. Padmanabhan, A. Sen Gupta, A. S. Gibbs, K. Mibu, S. Murai, J. M. Rondinelli, V. Gopalan, K. Tanaka and K. Fujita, *J. Am. Chem. Soc.*, 2018, **140**, 15690-15700.
18. S. Yoshida, K. Fujita, H. Akamatsu, O. Hernandez, A. Sen Gupta, F. G. Brown, H. Padmanabhan, A. S. Gibbs, T. Kuge, R. Tsuji, S. Murai, J. M. Rondinelli, V. Gopalan and K. Tanaka, *Advanced Functional Materials*, 2018, **28**, 1801856.
19. M. F. Liu, Y. Zhang, L. F. Lin, L. Lin, S. W. Yang, X. Li, Y. Wang, S. Z. Li, Z. B. Yan, X. Z. Wang, X. G. Li, S. Dong and J. M. Liu, *Appl. Phys. Lett.*, 2018, **113**, 022902.
20. N. A. Benedek, *Inorg. Chem.*, 2014, **53**, 3769-3777.
21. T. Zhu, T. Cohen, A. S. Gibbs, W. Zhang, P. S. Halasyamani, M. A. Hayward and N. A. Benedek, *Chem. Mater.*, 2017, **29**, 9489-9497.
22. T. Zhu, A. S. Gibbs, N. A. Benedek and M. A. Hayward, *Chem. Mater.*, 2020, **32**, 4340-4346.
23. S. Asaki, H. Akamatsu, G. Hasegawa, T. Abe, Y. Nakahira, S. Yoshida, C. Moriyoshi and K. Hayashi, *Jpn. J. Appl. Phys.*, 2020, **59**, 6.
24. M. A. Hayward, in *Comprehensive Inorganic Chemistry II*, eds. J. Reedijk and K. R. Poeppelmeier, Elsevier, Oxford, 2013, vol. 2, pp. 417-453.
25. T. Zhu, G. Khalsa, D. M. Havas, A. S. Gibbs, W. Zhang, P. Halasyamani, N. A. Benedek and M. A. Hayward, *Chem. Mater.*, 2018, **30**, 8915-8924.
26. S. Mallick, A. S. Gibbs, W. G. Zhang, P. S. Halasyamani, N. A. Benedek and M. A. Hayward, *Chem. Mater.*, 2020, **32**, 7965-7972.
27. S. Mallick, A. D. Fortes, W. Zhang, P. S. Halasyamani and M. A. Hayward, *Chem. Mater.*, 2021, **33**, 2666-2672.
28. S. Mallick, G. Khalsa, J. Z. Kaaret, W. Zhang, M. Batuk, A. S. Gibbs, J. Hadermann, P. S. Halasyamani, N. A. Benedek and M. A. Hayward, *Dalton Trans.*, 2021, **50**, 1539.
29. A. A. Coelho, Bruker AXS, Karlsruhe, Germany, 2016.
30. K. M. Ok, E. O. Chi and P. S. Halasyamani, *Chem. Soc. Rev.*, 2006, **35**, 710-717.
31. M. Shimazu, Y. Tanokura and S. Tsutsumi, *Japanese Journal of Applied Physics Part 1-Regular Papers Short Notes & Review Papers*, 1989, **28**, 1877-1881.
32. J. Gopalakrishnan, V. Bhat and B. Raveau, *Mater. Res. Bull.*, 1987, **22**, 413-417.
33. M. Sato, J. Abo, T. Jin and M. Ohta, *Solid State Ionics*, 1992, **51**, 85-89.
34. M. Sato, J. Abo, T. Jin and M. Ohta, *J. Alloys Compounds*, 1993, **192**, 81-83.
35. M. Jarvinen, *J. Appl. Crystallogr.*, 1993, **26**, 525-531.
36. N. E. Brese and M. O'Keeffee, *Acta Crystallogr., Sect. B : Strucut. Sci.*, 1991, **B47**, 192-197.
37. I. D. Brown and D. Altermatt, *Acta Crystallogr., Sect. B : Strucut. Sci.*, 1985, **B41**, 244-247.